Supporting Information

Electrocatalytic CO_2 Reduction to C_{2+} Products on CeO_2 Modified CuO Catalyst

Experimental Procedures

Materials

All chemicals are analytical grade and were used as purchased without further purification. The details are as follows: Copper (II) chloride ($CuCl_2 \cdot 2H_2O$, 99.5%, Sinopharm Chemical Reagent), diammonium cerium(IV) nitrate [$(NH_4)_2Ce(NO_3)_6$, 99.99%, J&K Reagent], NaOH (96%, Sinopharm Chemical Reagent), KOH (> 85%, Sinopharm Chemical Reagent), tetra-n-butylammonium hexafluorophosphate ($BminPF_6$, J&K Reagent), acetonitrile (CH_3CN, 99%, Sinopharm Chemical Reagent), CO_2 gas (> 99.999%, Guangming, Dalian, China). Ultrapure water is obtained by the ELGA filtering system.

Catalyst synthesis

In a typical procedure for the synthesis of precursor CeO_2/CuO, *x* M $CuCl_2 \cdot 2H_2O$ is dissolved in 15 mL water (labeled as solution **A**), and *y* M $(NH_4)_2Ce(NO_3)_6$ is dissolved in 15 mL water (labeled as solution **B**). The total amount of metal source is 0.075 M and the ratio of *y*:*x* equals to 10%, 20% or 30%. After mixing up **A** and **B**, 30 mL NaOH (0.8 M) was added dropwise into the mixture followed with another 1 h stirring. The obtained solution was then transferred into a 100 mL Teflon-lined stainless steel autoclave and was kept at 140 °C for 6 h. The resulting precipitate was collected by centrifugation, washed with distilled water and absolute ethanol, and finally dried in vacuum at 60 °C for 4 h.

Preparation of electrodes

The electrode was prepared by spraying the catalyst ink onto a hydrophobic gas diffusion electrode (YLS-30T, Suzhou Sinero Technology) with a mass loading of around 1.0 mg cm^{-2}. For the preparation of the catalyst ink, 40 mg catalyst, 40 μL 5 wt.% Nafion and 4 mL i-propanol were mixed and then sonicated for 30 min.

Materials characterizations

Samples were characterized by X-ray diffraction (XRD) on a Smartlab powder diffractometer using Cu Kα (λ = 1.5418 Å) radiation source. The morphologies were characterized with scanning electron microscopy (SEM, Hitachi Quanta 200F and Hitachi S5500) and transmission electron microscopy (TEM, Hitachi HT7700). Scanning transmission electron microscopy (STEM) images were performed on a JEOL JEM-F200 field-emission electron microscope equipped with an energy dispersive X-ray spectrometer (EDS). The high angle annular dark-field scanning transmission electron microscopy (HAADF-STEM) and corresponding energy dispersive spectroscopy (EDS) were performed with JEOL JEM-AFM 300F. X-ray photoelectron spectroscopy (XPS) measurements were conducted on a Thermofisher Escalab 250 Xi+ spectrometer with monochromated Al Kα excitation (1486.6 eV, 15 kV, 10.8 mA). For the elemental ICP measurements (ICP-AES, PerkinElmer Avio 550 Max), samples were dissolved by aqua regia. Temperature-programmed desorption measurements with a mass detector (TPD-MS) were carried out using a Micromeritics AutoChem 2920 system with a TCD detector coupling with an OmniStar 300 mass spectrometer.

Electrochemical active surface area (ECSA) measurement

ECSAs of the CeO_2/CuO and CuO catalysts were calculated from the double layer capacitance (C_{dl}) in the none-Faradic zone by conducting cyclic voltammetry (CV) tests under different scan rates. During the test, the CV curves were obtained in CH_3CN solution (0.1 M $BminPF_6$) saturated with Ar within a none-faradaic potential region. C_{dl} was determined by plotting the $\Delta J/2$ against the scan rates, where the ΔJ represents the difference between the anodic and cathodic current densities at a specific potential, 0.05 V *vs.* RHE for CeO_2/CuO and CuO, and 0 V *vs.* RHE for glassy carbon).

Electrochemical tests for CO_2RR

The CO_2RR tests were conducted in a three-chamber flow cell controlled by an electrochemical station (CHI 660e and CHI 1140C, Shanghai Chenhua Instruments). An Ag/AgCl electrode with salt bridge was used as reference electrode, and a Ni foil was used as the count electrode. All potentials were converted to RHE, otherwise noted.

The cathodic and anodic chambers were separated with an anion exchange membrane (fumasep FAA-3-PK-130). The dimension of the flow channel was 2 cm × 0.5 cm × 0.15 cm. The gas chamber was filled with CO_2 at a flow rate of 20 mL min^{-1}. 1 M KOH was used as the electrolyte. The catholyte was circulated into cathodic chamber through a peristaltic pump with a flow rate of 3.036 mL min^{-1}, while the anolyte was circulated by a gas-liquid mixing pump to reduce the disturbance of the produced oxygen. Before CO_2RR tests, all of the electrodes were pre-treated at −1.1 V *vs.* RHE (without *iR* correction) for 10 min in 1 M KOH under an identical condition.

Product analysis

Gas products (H_2, CO, CH_4 and C_2H_4) were quantified by an online gas chromatograph (GC, Agilent 7890A, Ar carrier and Agilent Parapok Q packed column) equipped with TCD (for H_2 detection), FID detectors and a methanizer (for CO and CH_x detection). The gas flowed through the electrochemical cell at a constant flow and was vented into the sampling loop of the GC. The Faradic efficiency of a certain gas product is calculated as follows:

$$FE_i = \frac{\frac{P}{RT} \times v_i \times n_i \times F}{I_{total}} \times 100\%$$

R: gas constant, 8.314 Pa m^3 mol^{-1} K^{-1};

v_i: gas flow rate of each gas product at room temperature, mL min^{-1};

n_i: electron transfer number;

F: Faraday constant, 96485 C mol^{-1};

I_{total}: total current given by electrochemical station, A;

Liquid products were analyzed by a Bruker AVANCE III 400 MHz nuclear magnetic resonance (NMR) spectrometer with dimethyl sulfoxide (DMSO) as the internal standard. The one dimensional ^1H spectrum was measured with water suppression using a presaturation method. The Faradic efficiency for a certain liquid product is calculated as follows:

$$FE_i = \frac{Q_i}{Q_{total}} \times 100\% = \frac{c_i \times V \times n_i \times F}{I_{total}} \times 100\%$$

c_i: concentration of the liquid products in the catholyte, mM；

V: total volume of the catholyte, mL；

Q_i: consumed charge of each liquid product, C；

Q_{total}: total charge accumulation during the electrolysis process, C；

DFT calculations

All calculations were carried out in Vienna Ab-initio Simulation Package (VASP) based on spin-polarized density functional theory (DFT).[1,2] The exchange–correlation energy was expressed by the generalized gradient approximation with Perdew–Burke–Ernzerhof (GGA-PBE) functional,[3] and the projector augmented wave (PAW) pseudopotential was used to represent core electrons effects.[4,5] A vacuum layer of 20 Å was introduced to eliminate interactions between periodic images. Due to the vacuum, dipole corrections were implemented. The cutoff energy was set to be 500 eV and Gaussian electron smearing method with σ = 0.05 eV were used. The empirical dispersion correction (DFT-D3) method was applied to describe the long-range van der Waals (vdW) interactions in layered materials.[6] DFT + U method was used to describe the electronic properties of Coulomb and exchange interactions of the strongly localized Ce-4f electrons, and the value of U for Ce was chosen as 5 eV.[5] The convergence tolerance for residual force and energy on each atom during structure relaxation were set to 0.02 eV/Å and 10^{-6} eV, respectively. The Monkhorst-Pack k-point mesh was set to be 3×3×1.

CeO_2/Cu is prepared as a kind of supported catalyst. The CeO_2/Cu model was built by placing a CeO_2 cluster on the Cu surface, and further optimization resulted in two optimized structures with different orientations of CeO_2 on the Cu surface (**Scheme S1**). After optimizing the reaction intermediates and adsorbates on the two optimized CeO_2/Cu models, the lower-energy structure (**Scheme S1a**) was used for further calculations.

The adsorption energy is calculated as:

$$\Delta E_{ads} = E_{*ads} - (E_{*} + E_{ads})$$

The water dissociation energy was calculated as:

$\Delta E_{dissociation} = E_{H2O*} - E_{H--OH*}$

Where, E_{*ads} is the electronic structure energy of the adsorbed on the catalyst, E_{*} is the energy of the slab, and E_{ads} is the energy in gas phase without the catalyst. The computational hydrogen electrode was used to model proton−electron pairs.[7]

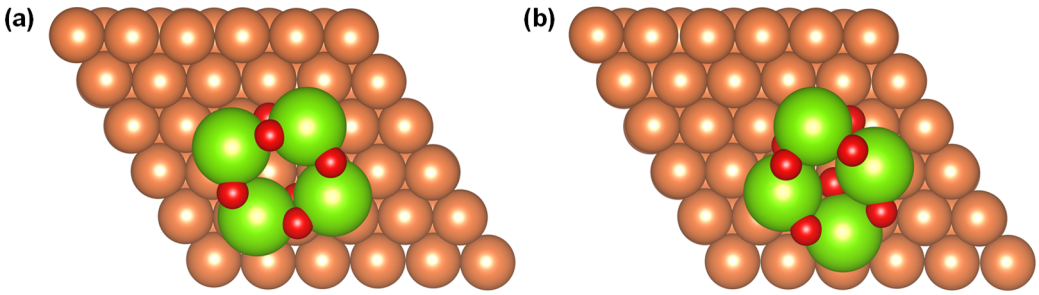

Scheme S1. Two optimized structures of CeO_2/Cu with different orientations of CeO_2 on the Cu surface.

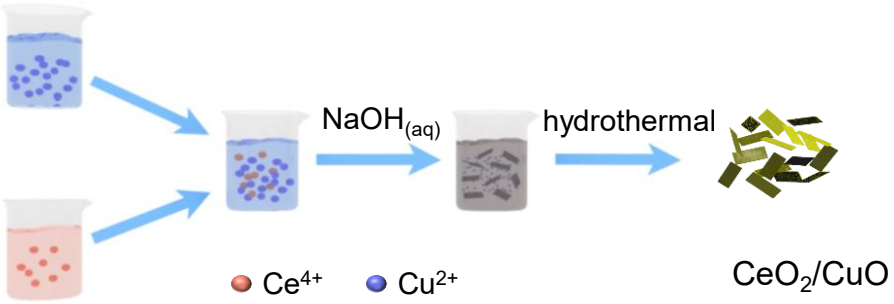

Figure S1. Schematic description of the synthesis of CeO_2/CuO.

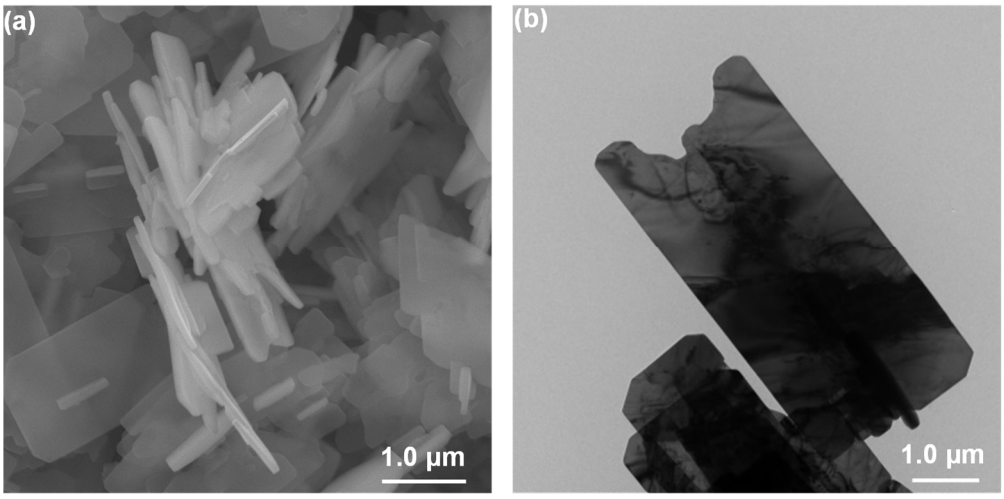

Figure S2. (a) SEM and (b) TEM images of CuO**.**

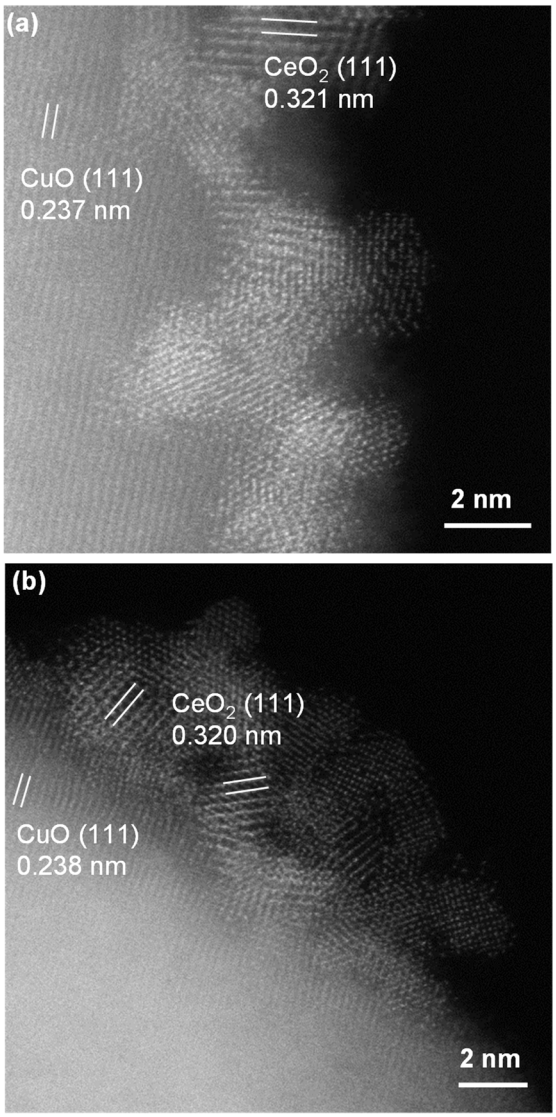

Figure S3. (a-b) HAADF-STEM images of 10%-CeO_2/CuO.

Table S1. The Ce:Cu molar ratio in the bulk of *x*%-CeO_2/CuO samples analyzed by ICP-AES.

samples	Ce:Cu molar ratio
10%-CeO_2/CuO	7.6%
20%-CeO_2/CuO	15.2%
30%-CeO_2/CuO	18.8%

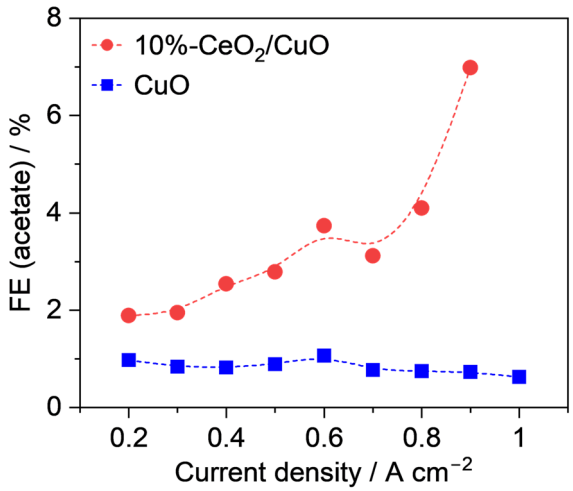

Figure S4. FE(acetate) of CuO and 10%-CeO_2/CuO for CO_2RR in a flow cell with 1 M KOH.

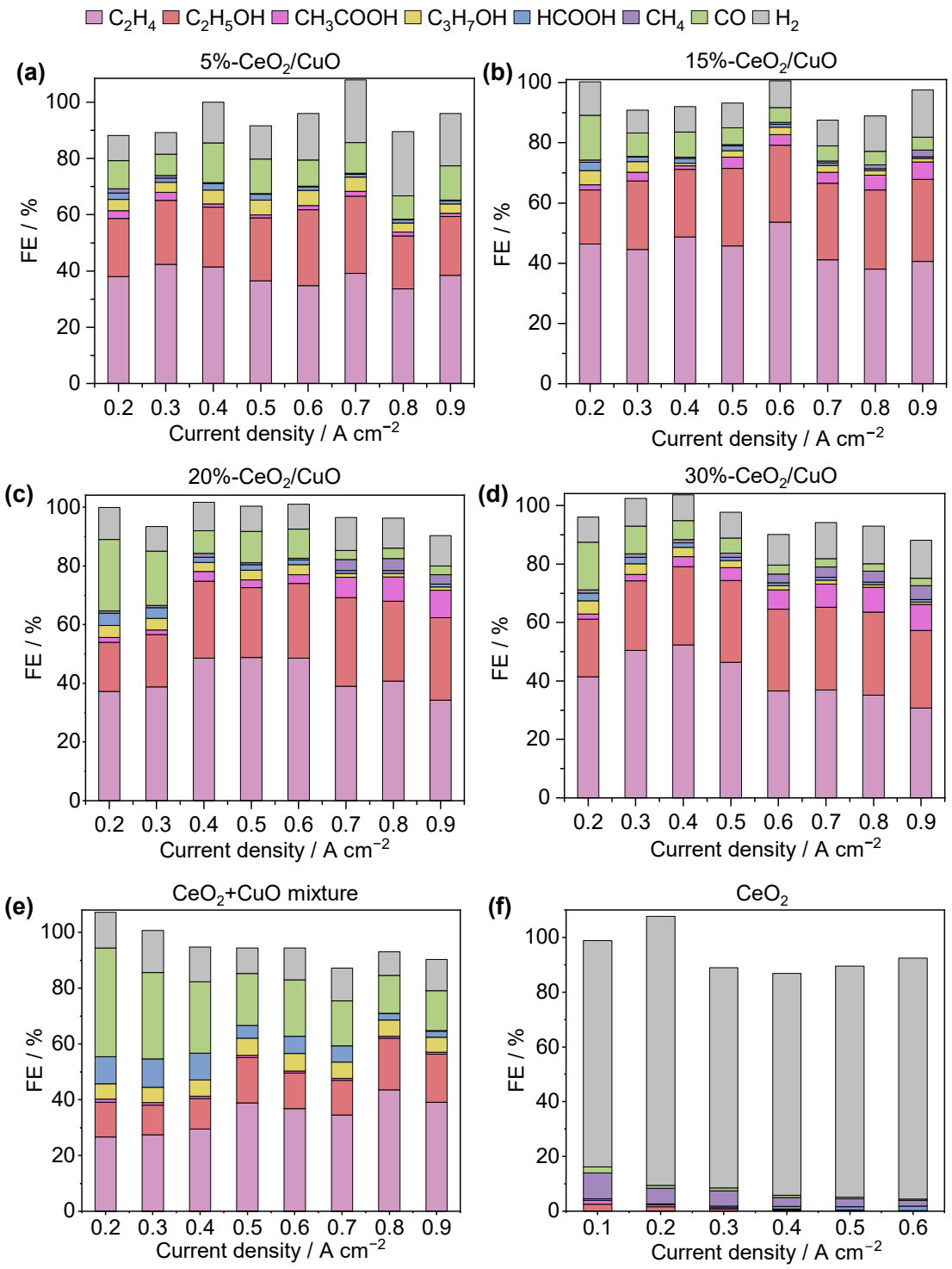

Figure S5. CO_2RR performances of (a) 5%-CeO_2/CuO, (b) 15%-CeO_2/CuO, (c) 20%-CeO_2/CuO, (d) 30%-CeO_2/CuO catalysts and (e) physically mixed CeO_2 and CuO catalysts (denoted as CeO_2+CuO mixture) with the Ce/Cu ratio equaling to that of 10%-CeO_2/CuO calculated from the ICP results, and (f) pure CeO_2 tested at different current densities in a flow cell with 1 M KOH as electrolyte.

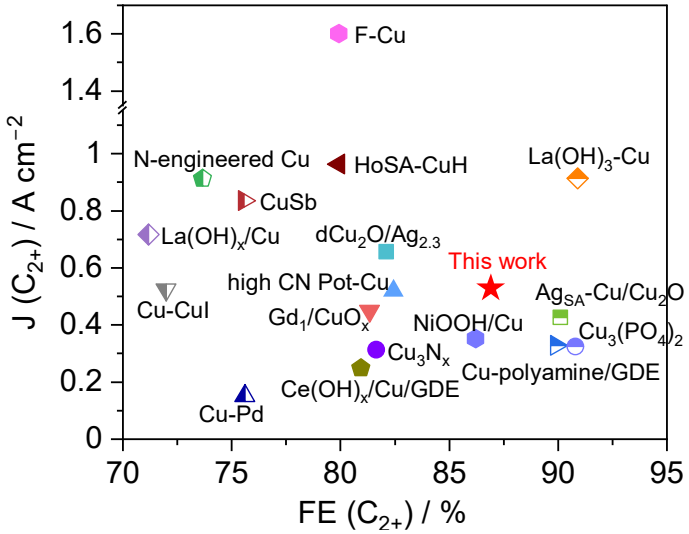

Figure S6. Comparison of the FE(C_{2+}) and J(C_{2+}) of this work and those in literatures.[8-24]

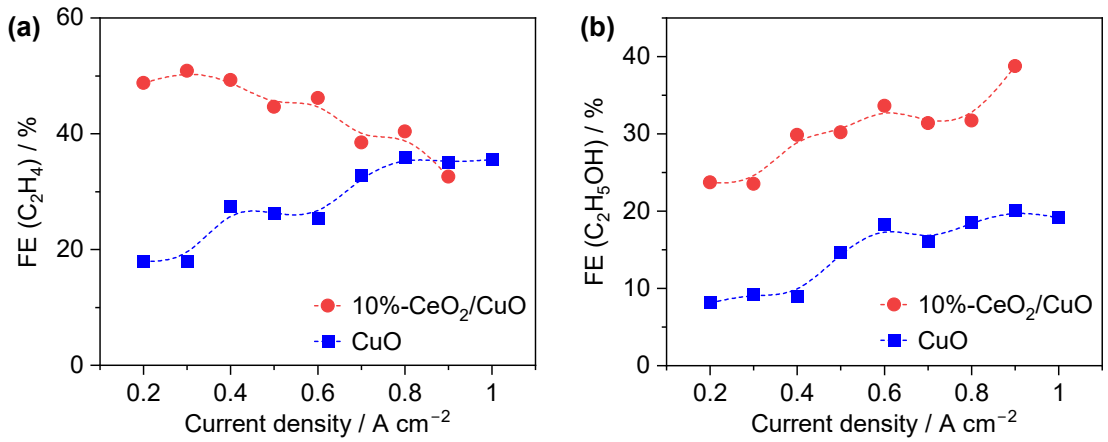

Figure S7. (a) FE(C_2H_4) and (b) FE(C_2H_5OH) of CuO and 10%-CeO_2/CuO for CO_2RR in a flow cell with 1 M KOH.

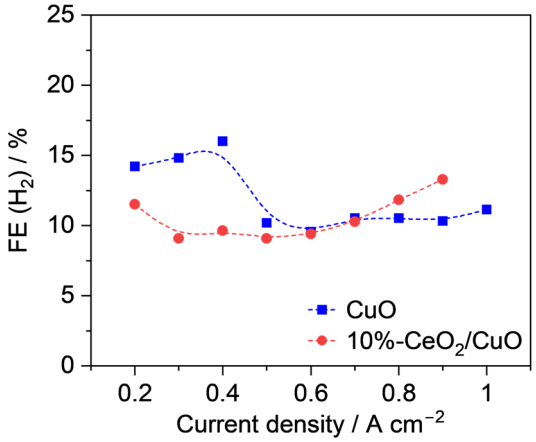

Figure S8. FE(H_2) of CuO and 10%-CeO_2/CuO for CO_2RR in a flow cell with 1 M KOH.

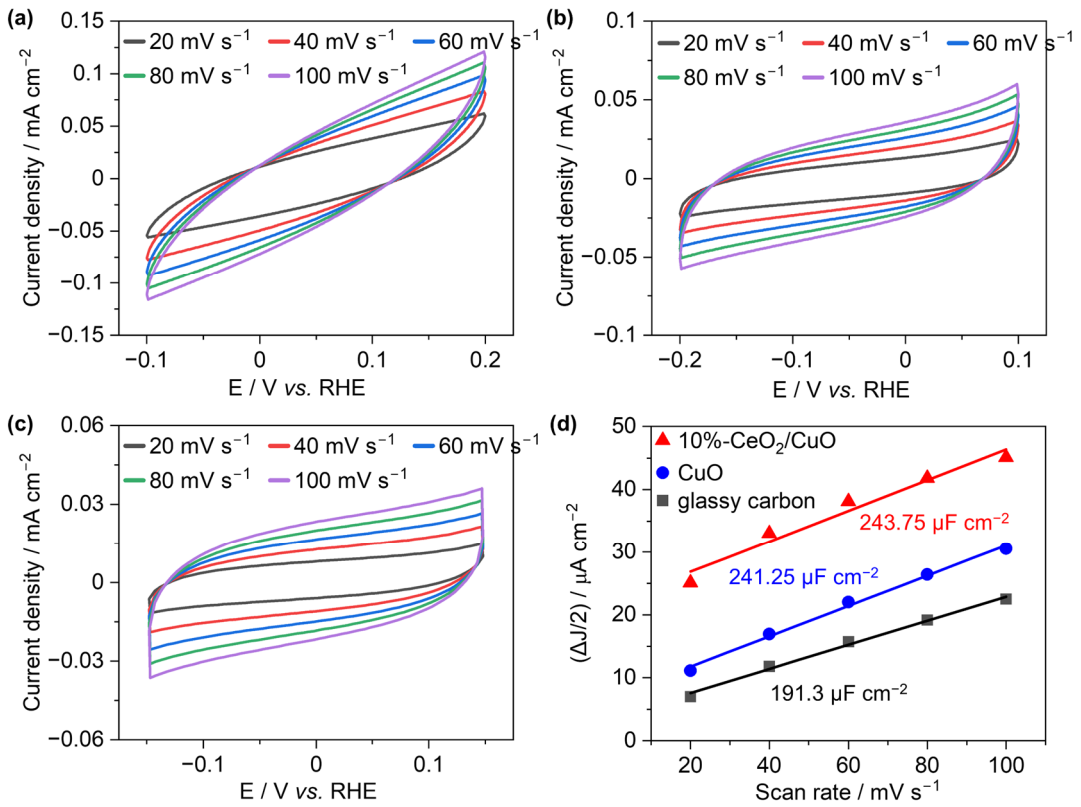

Figure S9. The CV curves of (a) 10%-CeO_2/CuO, (b) CuO and (c) glassy carbon in 1 M KOH. (d) Half of the capacitive current density of different catalysts in 1 M KOH as a function of scan rate over the non-faradic potential range.

Based on **Figure S9**, the calculated double-layer capacitances of 10%-CeO_2/CuO, CuO and glass carbon are 243.75, 241.25 and 191.3 μF cm^{-2}, respectively. Supposing the geometric area of the glassy carbon electrode is 1 cm^2, the relative electrochemical active surface area of 10%-CeO_2/CuO and CuO is 1.27 and 1.26 cm^2, respectively.

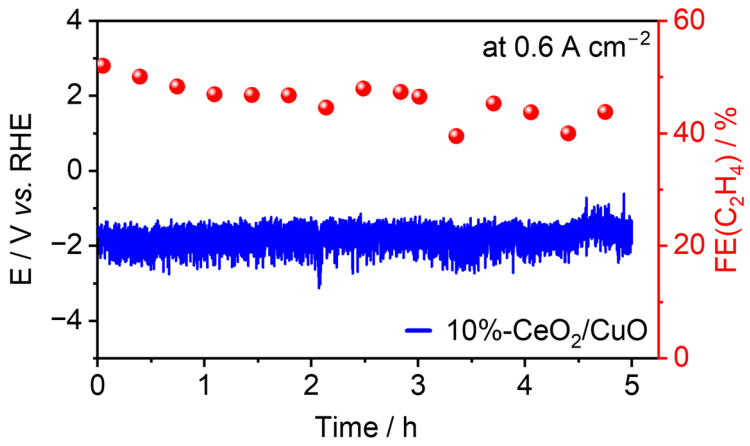

Figure S10. Stability test of 10%-CeO_2/CuO at a total current density of 0.6 A cm^{-2} in a flow cell.

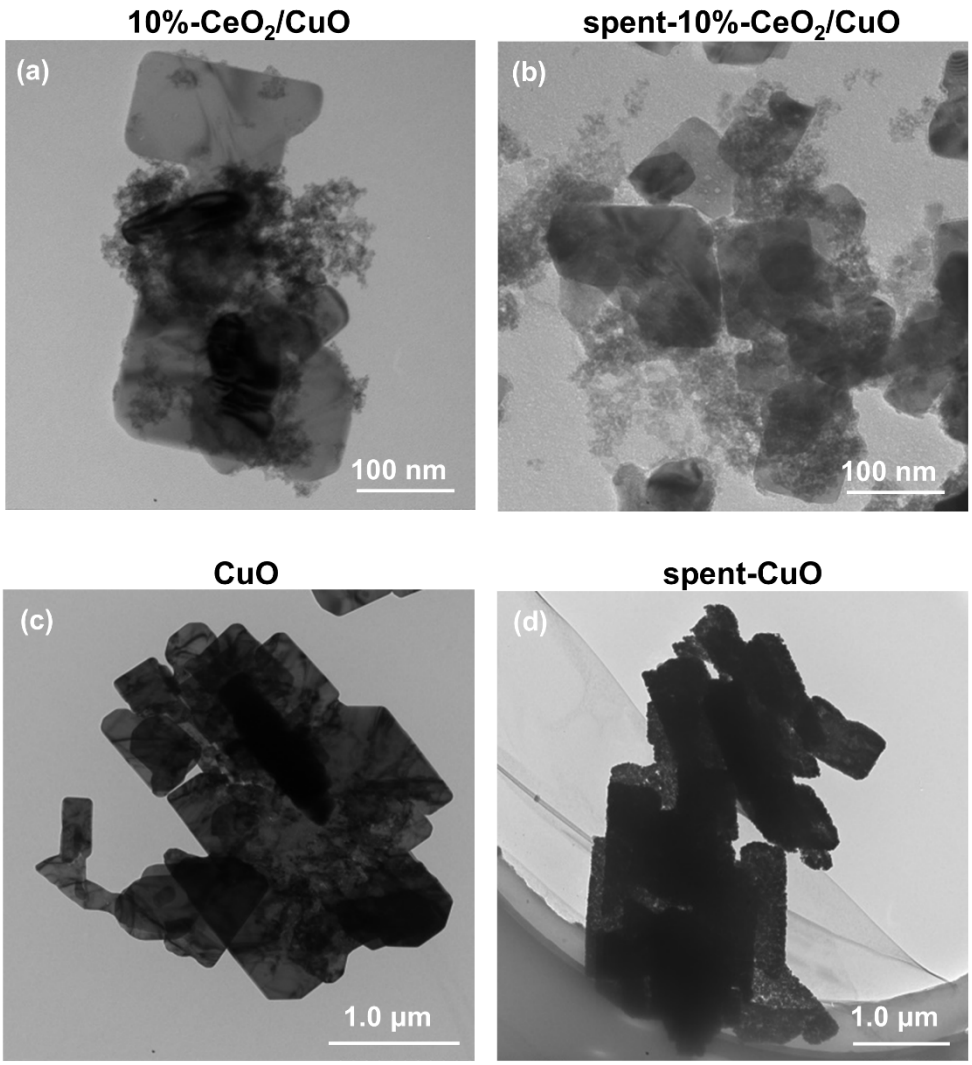

Figure S11. TEM images of 10%-CeO_2/CuO catalyst (a) before and (b) after CO_2RR. TEM images of CuO catalyst (c) before and (d) after CO_2RR.

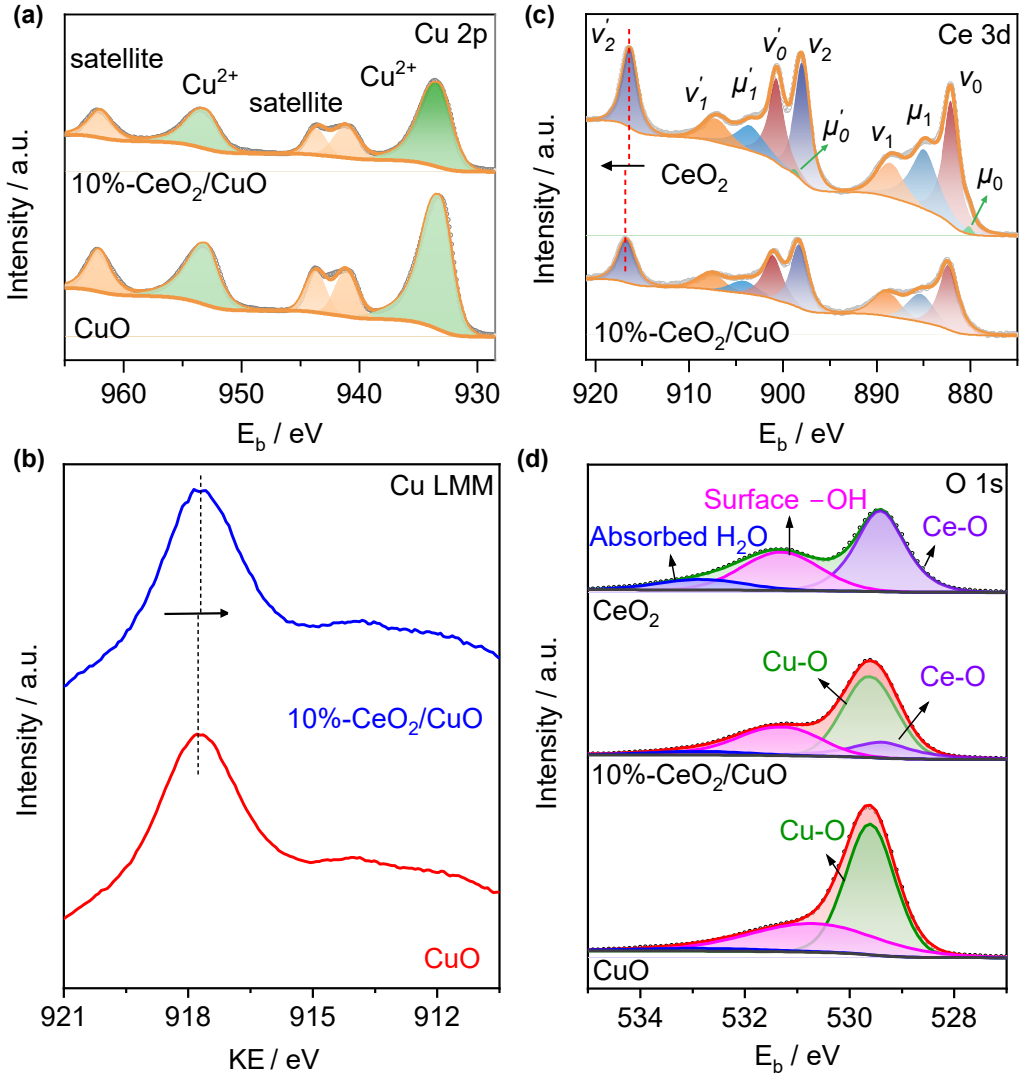

Figure S12. (a) Cu 2p XPS spectra and (b) Cu LMM Auger spectra of CuO and 10%-CeO_2/CuO. (c) Ce 3d XPS spectra of CeO_2 and 10%-CeO_2/CuO. (d) O 1s XPS spectra of CuO, 10%-CeO_2/CuO and CeO_2.

The Cu 2p spectrum of CuO and CeO_2/CuO show characteristic peak of Cu^{2+} at 933.6 eV, respectively. And there is a slight decrease of Cu LMM kinetic energy from 917.82 eV for CuO to 917.77 eV for CeO_2/CuO. This indicates a slightly decrease of Cu valence state upon introducing CeO_2.

The Ce 3d spectrum of CeO_2/CuO shows characteristic peaks of Ce^{4+} (ν_0, ν_1, ν_2, ν'_0, ν'_1, ν'_2) and Ce^{3+} (μ_0, μ_1, μ'_0, μ'_1),[25,26] consistent with those of CeO_2 sample. The well-defined single peak ν'_2 for CeO_2/CuO shifts to higher binding energy (~0.2 eV) compared with that for CeO_2.

Table S2. Ratios of Ce^{4+}/Ce^{3+} calculated from the XPS spectra of 10%-CeO_2/CuO and CeO_2.

	Ce^{4+}/Ce^{3+} (at.%)
10%-CeO_2/CuO	80.4%:19.6% (~4.0:1)
CeO_2	72.3%:27.7% (~2.6:1)

Table S3. Content of different oxygen species calculated from the O 1s XPS spectra (**Figure S12d**).

	10%-CeO_2/CuO	CeO_2
Ce−O (at.%)	15.9	52.0
Cu−O (at.%)	48.8	
Surface −OH (at.%)	29.5	36.6
Irreversibly absorbed H_2O (at.%)	5.8	11.4

The decreased content of adsorbed H_2O molecule and surface −OH compared with CeO_2 indirectly reflects the information of oxygen vacancies.[27] According to the literatures,[28,29] the O 1s XPS signals with a binding energy of 530 eV ~ 534 eV are ascribed to the irreversibly adsorbed H_2O (at 532.8 eV) and the surface hydroxyls (at 531.3 eV) resulting from the dissociative water adsorption at the oxygen vacancy site according to the equation $H_2O_{(g)} + V_O + O_{(s)} \rightarrow 2^*OH$. Since the XPS measurement was conducted under high vacuum conditions, the signals cannot originate from the atmospheric species. Therefore, the O 1s XPS signals of –H_2O and –OH species, especially –OH, are closely related to the existence of oxygen vacancies.

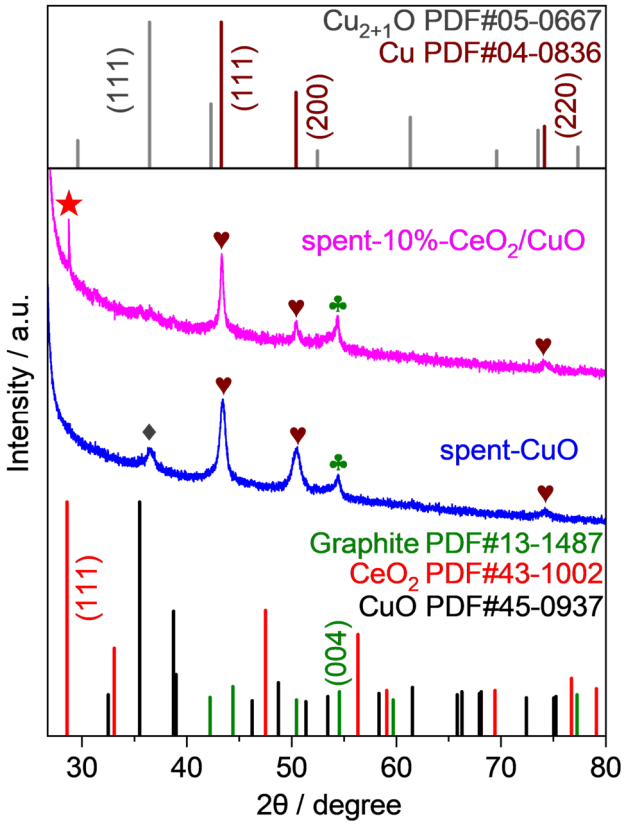

Figure S13. XRD patterns of CuO and 10%-CeO_2/CuO after 1 h electrolysis at a total current density of 0.6 A cm^{-2}, with detailed comparison with the standard patterns of possible phases (Cu, CuO, CeO_2, graphite and $Cu_{2+1}O$). In order to detect the XRD patterns better, the loading amount of these catalysts for XRD measurements is doubled to 2 mg cm^{-2}.

After the reaction, the signals of CuO disappear. Spent-CuO shows a weak diffraction peak at 36.44°, which is corresponding to (111) facet of $Cu_{2+1}O$, resulting from the rapid oxidation of Cu in air. However, this peak is negligible for spent-10%-CeO_2/CuO, which may benefit from the interaction and the synergistic effect between CeO_2 and Cu, explaining the improved structural stability of 10%-CeO_2/CuO (**Fig. S11a-b**).

Note: the graphite signals of two samples come from the GDE substrate.

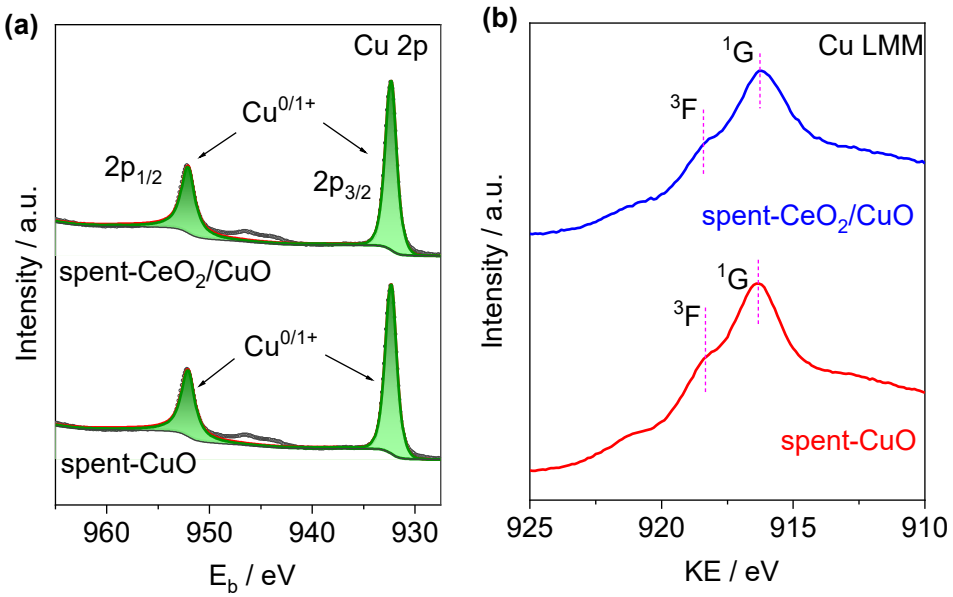

Figure S14. (a) Cu 2p XPS spectra and (b) Cu LMM Auger spectra of 10%-CeO_2/CuO and CuO after 1 h electrolysis at a total current density of 0.6 A cm^{-2}.

According to the literatures,[30-32] Cu LMM Auger spectrum usually splits into two final-state terms, namely ^1G and ^3F, due to the L-S coupling effect, and ^3F peak is only observed for Cu^0. **Figure S14b** shows that ^3F peak can be observed for both spent-CeO_2/CuO and spent-CuO, verifying the existence of metallic Cu^0.

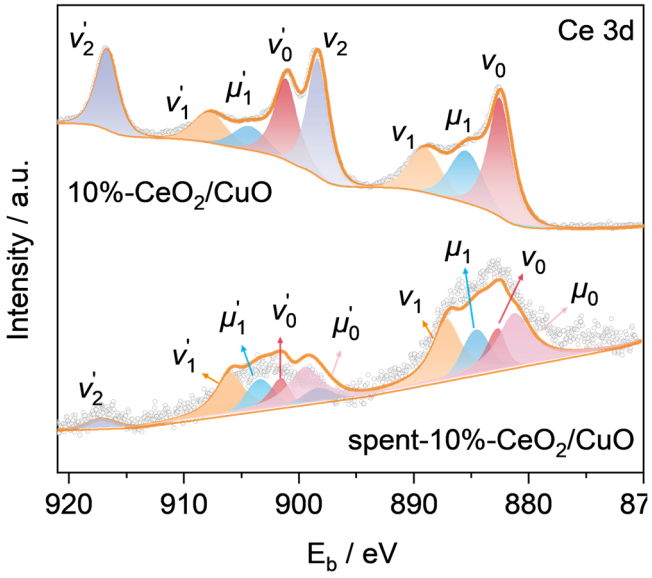

Figure S15. Ce 3d XPS spectra of 10%-CeO_2/CuO before and after 1 h electrolysis at a total current density of 0.6 A cm^{-2}.

Table S4. Ratios of Ce^{4+}/Ce^{3+} calculated from the XPS spectra of 10%-CeO_2/CuO before and after electrolysis.

	10%-CeO_2/CuO	spent-10%-CeO_2/CuO
Ce^{3+} (at.%)	19.2	48.9
Ce^{4+} (at.%)	80.8	51.1
Ce^{4+}/Ce^{3+}	4.2:1	1.0:1

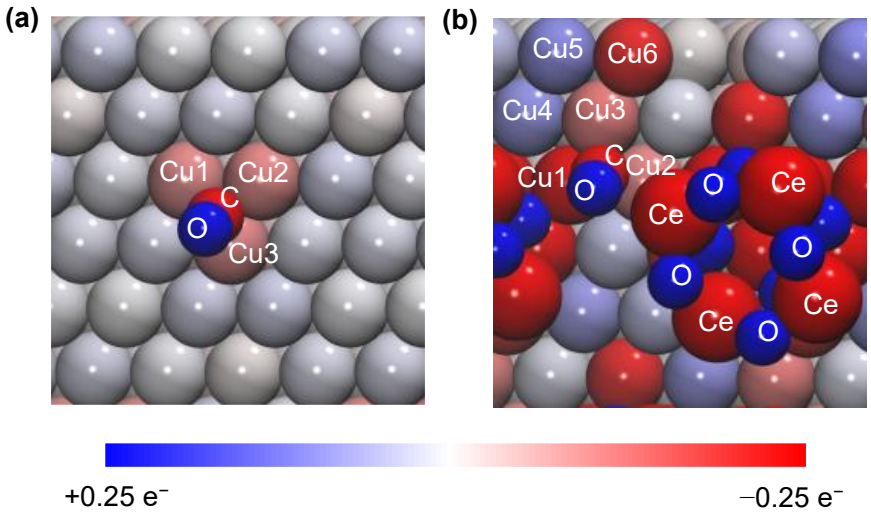

Figure S16. Charge variation of *CO adsorbed on (a) Cu and (b) CeO_2/Cu. (positive value indicates accepting electrons, and negative value indicates losing electrons).

Table S5. Bader charge calculation results of *CO adsorbed on Cu and CeO_2/Cu.

	Atoms	Charge variation of Cu@CO	Atoms	Charge variation of CeO_2/Cu@CO
Surface	Cu1	−0.1081	Cu1	−0.3589
	Cu2	−0.1099	Cu2	−0.1120
	Cu3	−0.1099	Cu3	−0.1278
			Cu4	0.0990
			Cu5	0.1080
			Cu6	−0.2179
Absorbed species	C	−1.4772	C	−1.3194
	O	1.8365	O	1.9490

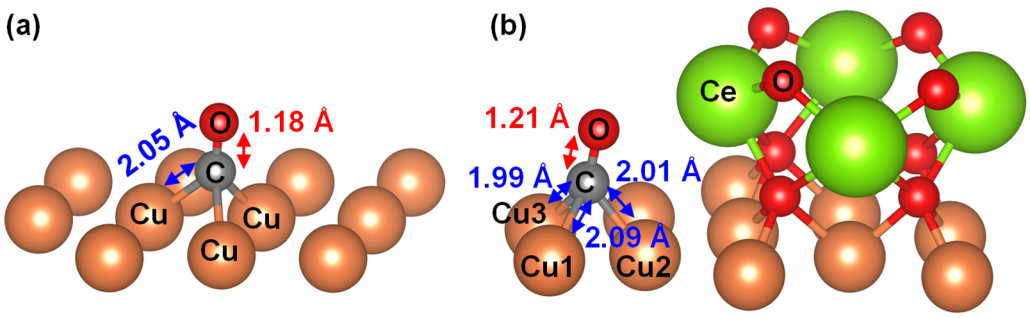

Figure S17. Structure models of *CO adsorbed on (a) Cu and (b) CeO_2/Cu.

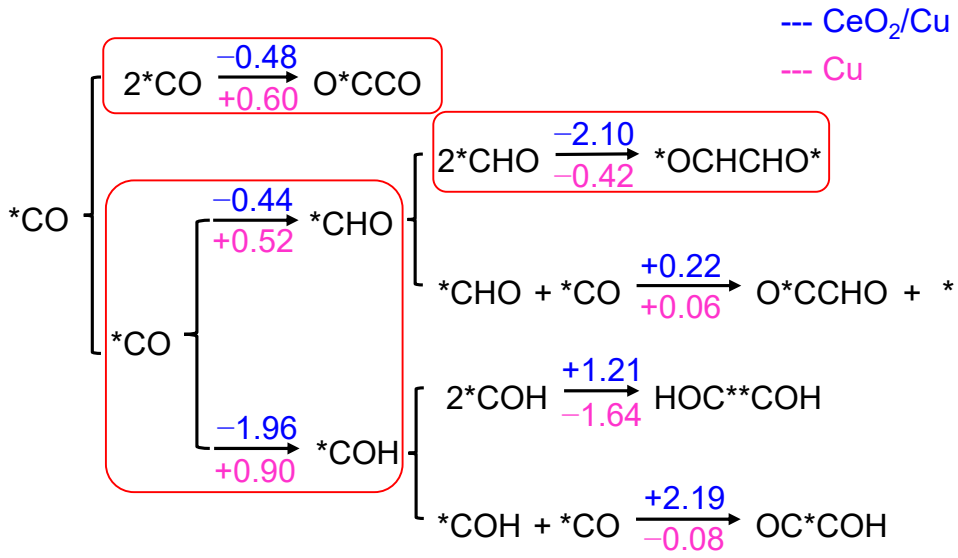

Figure S18. The changes of adsorption energy (ΔE_{ads}) for different C−C coupling pathways. The pink and blue numbers represented the ΔE_{ads} on Cu and CeO_2/Cu surfaces, respectively.

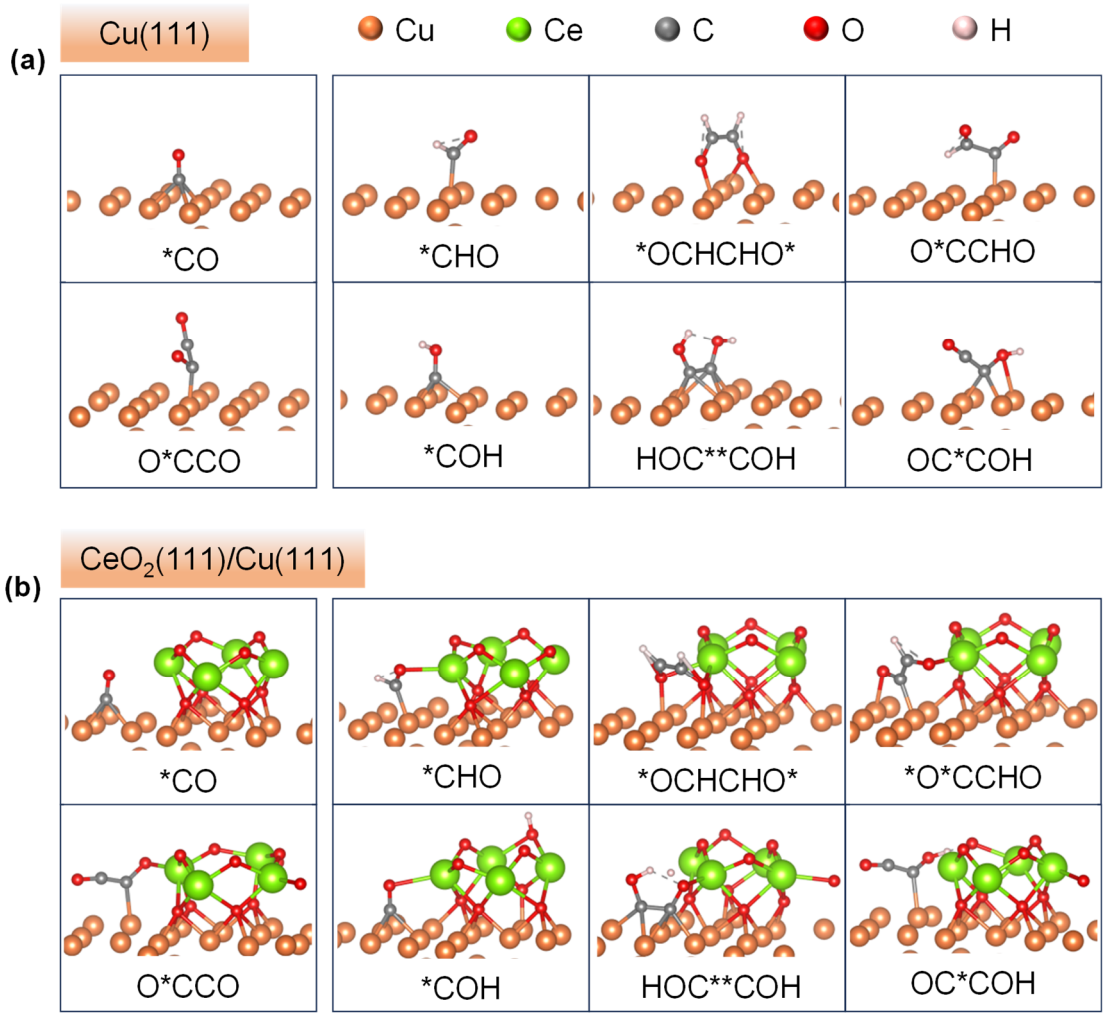

Figure S19. The optimized structures of key intermediate during the possible C–C coupling process on Cu(111) and CeO_2(111)/Cu(111).

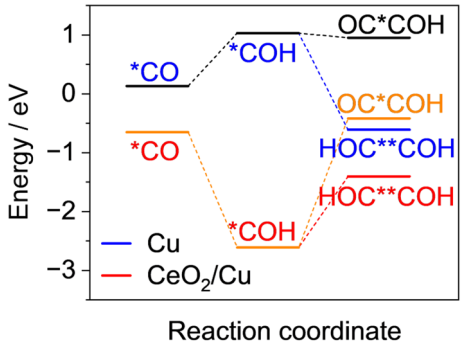

Figure S20. The reaction energy diagrams for the CO_2RR to describe the possible C–C coupling steps from *CO on Cu and CeO_2/Cu.

References

1 G. Kresse and J. Furthmüller, *Comput. Mater. Sci.*, 1996, **6**, 15-50.

2 G. Kresse and J. Furthmüller, *Phys. Rev. B*, 1996, **54**, 11169-11186.

3 J. P. Perdew, K. Burke and M. Ernzerhof, *Phys. Rev. Lett.*, 1996, **77**, 3865-3868.

4 G. Kresse and D. Joubert, *Phys. Rev. B*, 1999, **59**, 1758-1775.

5 P. E. Blöchl, *Phys. Rev. B*, 1994, **50**, 17953-17979.

6 S. Grimme, J. Antony, S. Ehrlich and H. Krieg, *J. Chem. Phys.*, 2010, **132**, 154104.

7 Q. Tan, H. Zhu, S. Guo, Y. Chen, T. Jiang, C. Shu, S. Chong, B. Hultman, Y. Liu and G. Wu, *Nanoscale*, 2017, **9**, 12565-12572.

8 C. Peng, G. Luo, Z. Xu, S. Yan, J. Zhang, M. Chen, L. Qian, W. Wei, Q. Han and G. Zheng, *Adv. Mater.*, 2021, **33**, 2103150.

9 X. Lang, Z. Zhu, W. Guo, G. Xie, D. Liu, W. Gao, Q. Gong, Y. Zhai and X. Lu, *Angew. Chem. Int. Ed.*, 2025, **64**, e17221.

10 J. Feng, L. Wu, S. Liu, L. Xu, X. Song, L. Zhang, Q. Zhu, X. Kang, X. Sun and B. Han, *J. Am. Chem. Soc.*, 2023, **145**, 9857-9866.

11 J. Jiao, X. Kang, J. Yang, S. Jia, Y. Peng, S. Liu, C. Chen, X. Xing, M. He, H. Wu and B. Han, *J. Am. Chem. Soc.*, 2024, **146**, 15917-15925.

12 P. Li, J. Liu, Y. Wang, X.-D. Zhang, Y. Hou, Y. Zhang, X. Sun, X. Kang, Q. Zhu and B. Han, *J. Am. Chem. Soc.*, 2024, **146**, 26525-26533.

13 M. Zheng, P. Wang, X. Zhi, K. Yang, Y. Jiao, J. Duan, Y. Zheng and S.-Z. Qiao, *J. Am. Chem. Soc.*, 2022, **144**, 14936-14944.

14 X. Chen, J. Chen, N. M. Alghoraibi, D. A. Henckel, R. Zhang, U. O. Nwabara, K. E. Madsen, P. J. A. Kenis, S. C. Zimmerman and A. A. Gewirth, *Nat. Catal.*, 2020, **4**, 20-27.

15 P. Wang, H. Yang, C. Tang, Y. Wu, Y. Zheng, T. Cheng, K. Davey, X. Huang and S.-Z. Qiao, *Nat. Commun.*, 2022, **13**, 3754.

16 C. Zhu, A. Chen, J. Mao, G. Wu, S. Li, X. Dong, G. Li, Z. Jiang, Y. Song, W. Chen and W. Wei, *Small Struct.*, 2023, **4**, 2200328.

17 W. Ma, S. Xie, T. Liu, Q. Fan, J. Ye, F. Sun, Z. Jiang, Q. Zhang, J. Cheng and Y. Wang, *Nat. Catal.*, 2020, **3**, 478-487.

18 M. Luo, Z. Wang, Y. C. Li, J. Li, F. Li, Y. Lum, D.-H. Nam, B. Chen, J. Wicks, A. Xu, T. Zhuang, W. R. Leow, X. Wang, C.-T. Dinh, Y. Wang, Y. Wang, D. Sinton and E. H. Sargent, *Nat. Commun.*, 2019, **10**.

19 S. Hu, Y. Chen, Z. Zhang, S. Li, H. Liu, X. Kang, J. Liu, S. Ge, J. Wang, W. Lv, Z. Zeng, X. Zou, Q. Yu and B. Liu, *Small*, 2024, **20**, 2308226.

20 X. Mao, C.-W. Chang, Z. Li, Z. Han, J. Gao, M. Lyons, G. Sterbinsky, Y. Guo, B. Zhang, Y. Wang, X. Wang, D. Han, Q.-H. Yang, Z. Feng and Z. Weng, *Adv, Energy Mater.*, 2024, **14**, 2400827.

21 H. Li, T. Liu, P. Wei, L. Lin, D. Gao, G. Wang and X. Bao, *Angew. Chem. Int. Ed.*, 2021, **60**, 14329-14333.

22 X. Y. Zhang, Z. X. Lou, J. Chen, Y. Liu, X. Wu, J. Y. Zhao, H. Y. Yuan, M. Zhu, S. Dai, H. F. Wang, C. Sun, P. F. Liu and H. G. Yang, *Nat. Commun.*, 2023, **14**, 7681.

23 Z. Zhang, Q. Fang, X. Yang, S. Zuo, T. Cheng, Y. Yamauchi and J. Tang, *Adv. Mater.*, 2025, **37**, 2411498.

24 H. Zhang, S. Liu, C. Zhang, W. Liu, H. Dong, Z. Shi, H. Xu, J. Liu, D. Wang, J. Jiao, M. Gao and T. Lu, *Angew. Chem. Int. Ed.*, 2026, **65**, e18519.

25 P. Burroughs, A. Hamnett, A. F. Orchard and G. Thornton, *Dalton Trans.*, 1976, 1686-1698.

26 Y. Wang, Z. Chen, P. Han, Y. Du, Z. Gu, X. Xu and G. Zheng, *ACS Catal.*, 2018, **8**, 7113-7119.

27 H. Idriss, *Surf. Sci.*, 2021, **712**, 121894.

28 T. J. Frankcombe and Y. Liu, *Chem. Mater.*, 2023, **35**, 5468-5474.

29 A. Posada-Borbón, N. Bosio and H. Grönbeck, *Surf. Sci.*, 2021, **705**, 121761.

30 H. Wu, J. Li, K. Qi, Y. Zhang, E. Petit, W. Wang, V. Flaud, N. Onofrio, B. Rebiere, L. Huang, C. Salameh, L. Lajaunie, P. Miele and D. Voiry, *Nat. Commun.*, 2021, **12**, 7210.

31 M. Fang, M. Wang, Z. Wang, Z. Zhang, H. Zhou, L. Dai, Y. Zhu and L. Jiang, *J. Am. Chem. Soc.*, 2023, **145**, 11323-11332.

32 W. Zhang, C. Huang, Q. Xiao, L. Yu, L. Shuai, P. An, J. Zhang, M. Qiu, Z. Ren and Y. Yu, *J. Am. Chem. Soc.*, 2020, **142**, 11417-11427.